Pergamon

Int. J. Heat Mass Transfer. Vol. 40, No. 18, pp. 4263–4271, 1997

Printed in Great Britain
0017–9310/97 $17.00+0.00

PII: S0017–9310(97)00091–4

Mass-transfer to a channel wall downstream of a cylinder

J. DELIANG YANG,† AHMED SHEHATA,‡ VIJAY MODI‡ and ALAN C. WEST†§

† Department of Chemical Engineering, Materials Science and Mining Engineering, Columbia University, New York, NY 10027, U.S.A.

‡ Department of Mechanical Engineering, Columbia University, New York, NY 10027, U.S.A.

(*Received* 22 *August* 1996 *and in final form* 21 *March* 1997)

Abstract—The electrochemical method is used to measure the mass-transfer to a channel wall downstream of a cylinder. For Reynolds numbers based on cylinder diameter $Re > 50$, the flow is unsteady, and the mass-transfer rate is a function of time. When $50 < Re < 200$, the mass-transfer rate is periodic with a frequency in the range of 1–3 Hz. When the ratio of cylinder diameter d to channel height h is 0.25, the Strouhal number is measured to be 0.27 ± 0.02, and when $d/h = 0.51$, the Strouhal number is 0.49 ± 0.01. The average mass-transfer rate at various positions downstream of the cylinder is reported. Experiments are compared to two-dimensional numerical simulations. The simulated and experimental variations of Nusselt number with position and Re contain similar features, but exact agreement is not found. © 1997 Elsevier Science Ltd.

INTRODUCTION

Electrodeposited metallic and alloy films have a wide range of industrial applications. Applications in the computer industry require high quality of the deposits in terms of thickness uniformity, for example. Processes attempt to employ mixing methods that allow high metallization rates within a strict spatial-uniformity requirement. For example, the paddle cell designed by Romankiw [1] produces highly uniform deposits at high metallization rates and is used extensively for magnetic-storage applications. Schwartz *et al.* [2] studied the paddle cell and observed that the wake trailing the paddle interacts with the diffusion layer at the cathode and induces periodic plating. An understanding of mass-transfer rates behind bluff bodies may enable the development of other mixing methods for high-end metallization applications.

Enhanced rate of mass-transfer in the wake region behind a bluff body has long been recognized [3–8]. The mass-transfer rate was shown to be greatly enhanced by placing multiple cylinders near the outer edge of a boundary layer [3, 4]. The rate of mass-transfer was found to depend on the flow rate, the spacing between the cylinder and the plane, and the separation distances between cylinders. The enhanced rate of mass-transfer persists for over 130 diameters downstream of the cylinders. The effect of cylinders on heat and mass-transfer rates through flowing liquid films has also been investigated [7]. The use of cylinders in a flow channel to enhance mass-transfer rate has also been applied to electrodialysis [5, 6]. Enhancement of heat transfer from the heated wall of a two-dimensional (2-D) channel due to a cylinder has been investigated by Karniadakis *et al.* [9], Kozlu *et al.* [10] and Yesilyurt and Patera [11]. A recent study by Myrum *et al.* [12] reports the use of a cylinder as an eddy promoter for transport enhancement in a channel with a ribbed lower wall.

The vortex shedding phenomena downstream of a cylinder has also been studied extensively. A cylinder in a free stream has received the most attention. For this case, the flow is found to be steady for $Re < 50$ and periodic for $50 < Re < 194$. In a free stream, the natural shedding frequency reported in terms of the Strouhal number is approximately 0.2. At higher flow rates, the appearance of three-dimensional (3-D) vortices has been observed. A detailed review of vortex dynamics behind a cylinder is given by Williamson [13].

The present paper reports an experimental and computational study of mass-transfer to a channel wall downstream of a cylinder. The electrochemical method is used for the measurements [14, 15]. The rate of mass-transfer was recorded at various locations. Two ratios of cylinder diameter to cell height and three positions of the cylinder in the channel were studied.

EXPERIMENTAL

Channel design

A flow channel was designed to satisfy three criteria. First, the fluid flow is well-defined and can be simulated (over a reasonable range of flow rates). Second, the material used for the channel is inert with respect to the fluid. Finally, the channel dimensions allow

§ Author to whom correspondence should be addressed.

NOMENCLATURE

b	distance between bottom wall and cylinder center [cm]
c	concentration [mol cm^{-3}]
d	diameter of cylinder [cm]
D	diffusion coefficient [cm^2 s^{-1}]
f	frequency of oscillation [Hz]
F	Faraday's constant, 96,487 [C mol^{-1}]
h	channel height [cm]
i	current density [mA cm^{-2}]
L	electrode half length [cm]
Nu	Nusselt number
P	pressure [N cm^{-2}]
Re_h	Reynolds number based on the channel height
Re	Reynolds number based on cylinder diameter
S	Strouhal number, fd/u_{avg}
Sc	Schmidt number, v/D
t	time [s]
u	velocity [cm s^{-1}]
u_m	experimental average velocity in the x-direction [cm s^{-1}]
u_{avg}	average velocity in the sensor region of the cell [cm s^{-1}]
u_{max}	maximum velocity in the x-direction [cm s^{-1}]
w	width of the channel [cm]
x, y	Cartesian coordinate [cm].

Greek symbols

β	shear at a wall [s^{-1}]
ν	kinematic viscosity [cm^2 s^{-1}]
ρ	density [kg cm^{-3}]
τ	period of oscillation or sampling time [s].

Subscripts

avg	time or spatial average
no	results when no cylinder is present
x, y	x or y component
∞	bulk value.

access to the electrodes and are sufficiently small to avoid the use of an excessive volume of electrolyte. A schematic of the design is shown in Fig. 1.

The cell was constructed of transparent Plexiglas. The channel has cross-sectional dimensions of $h \times w = 1.86 \times 9.53$ cm and is 132.1 cm long. The contoured entrance and exit regions of length 15.24 cm help minimize entrance or exit effects. The mass-transfer sensor is located 68.58 cm downstream of the inlet region. For the designed system, a fully developed flow at the blocking cylinder should be obtained for all $Re_h < 1600$ [16].

Natarajan and Lakshmanan [17] curve fit numerical and experimental results for the fully developed velocity profile in finite-aspect ratio channels to obtain

$$\frac{u_x}{u_{max}} = \left[1 - \left(\frac{2y}{h} - 1\right)^2\right]\left[1 - \left|\frac{2z}{w}\right|^m\right] \quad (1)$$

where $m = 1.7 + 0.5\,(h/w)^{-1.4}$ for $h/w \leqslant 1/3$, y and z are the coordinates perpendicular to the flow (see Fig. 2), with origin placed at the center of the bottom wall. The mass-transfer sensor is positioned between $-0.11 < z/w < 0.11$, and is thus inside the region of an essentially two-dimensional flow. The measured, volumetric flow rate Q is related to the mean fluid velocity u_m through $Q = whu_m$. The average velocity u_{avg} in the region of the sensor is higher than u_m due to edge effects. For the aspect ratio of the present channel,

$$u_m = 0.87u_{avg}. \quad (2)$$

The inlet connection to the cell is made with 1/4 in ID Nalgene Premium tubing. To avoid pressure build-up in the cell, larger tubing (1/2 in ID) is used at the

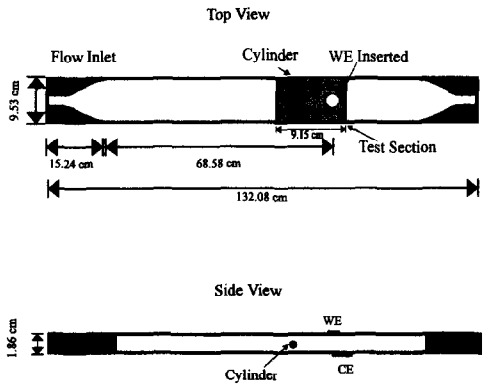

Fig. 1. Experimental setup. The contoured entrance and exit regions help minimize entrance or exit effects. Electrolyte is pumped into the channel from left to right. A cylinder of diameter d is placed upstream of the sensor.

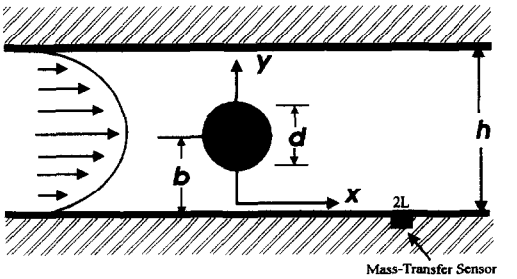

Fig. 2. Schematic of the cell. The working electrode of length $2L$ is placed downstream a distance x from a cylinder of diameter d. The center of the cylinder is positioned a distance b from the bottom wall.

outlet. An electrolyte flow is provided with a variable-speed gear pump (Gear Pump-Model 221-56c, Cole Parmer Instrument Company). Flow rates of 10–120 $cm^3\ s^{-1}$ were normally used. Lower flow rates were obtained with a smaller centrifugal pump (Model AC-2CP-MD, March MFG, Inc.)

The mass-transfer sensor (labeled WE in Fig. 1) was made of 0.01×2.00 cm platinum foil, cast in a cylindrical mold. The mold was mounted flush to the center of a plate. The entire plate was flush mounted to the channel so that the electrode is perpendicular to the flow direction. The counterelectrode (labeled CE in Fig. 1) was made of 2×6 cm nickel foil mounted to a removable plate located on the wall opposite the sensor. An electrical connection was made to the electrode via a hole through the plate. The counterelectrode, which is positioned slightly downstream of the working electrode, also served as the reference electrode.

A cylinder of uniform diameter was placed upstream of the mass-transfer sensor. A small spring was attached to one end of the cylinder to secure it to holes drilled on two demountable plates on the side walls (not shown in Fig. 1). The location of the cylinder is adjusted by using plates with holes at different positions. Cylinders with diameters of 0.465 and 0.953 cm, corresponding to a cylinder-diameter/cell-height ratio of 0.25 and 0.51, were used. The cylinder was placed at distances of 0.9, 1.9 and 3.9 cm upstream of the center of the sensor. The uncertainty in cylinder position is ± 0.05 cm.

Solution chemistry and measurement procedure

The experiments used 7 l of electrolyte composed of 0.003 M potassium ferricyanide, 0.003 M potassium ferricyanide and 0.1 M potassium chloride. The reduction of ferricyanide ion takes place at the sensor and the reverse reaction takes place at the anode. The temperature was 23 ± 2°C. The diffusivity of the ferricyanide ion was determined from experiments in the channel in the absence of a cylinder and was found to be $D = 0.8 \times 10^{-5}\ cm^2\ s^{-1}$. This value is in accord with a value of $0.896 \times 10^{-5}\ cm^2\ s^{-1}$ reported for infinitely dilute solutions [18].

The flow rate was determined from the time required to accumulate 2 l of solution in a graduated cylinder. Prior to pumping electrolyte into the channel, the working electrode was polished down to 600 grit with sandpaper and rinsed with deionized water several times. The channel was also cleaned with distilled water before rinsing the channel with the electrolyte. The fluid was then pumped into the channel, care being taken to remove air bubbles and to eliminate leaks.

Measurements were taken after about 5 min of a constant volumetric flow rate. Sampling frequency was set at 1000 Hz for 30 s for each experiment. To reduce noise, 30 successive points were averaged together. The flow rate was varied from low to high flow rates. At the completion of the highest flow rate studied, the position of the cylinder was changed.

A Pine Instruments AFRDE4 potentiostat was used to control potential and measure current. The potential was set at the limiting-current plateau, typically it is set at an overpotential of -200 mV vs the comparison electrode. A LPCLAB DT-2811 A/D board was connected to a computer to record the current as a function of time.

NUMERICAL SIMULATIONS

A schematic of the cell is shown in Fig. 2. In the theoretical analysis, it is assumed that $h \ll w$ (see Fig. 1). A cylinder of diameter d is placed a distance b from the bottom wall, and the working electrode of length $2L$ is placed at a distance x downstream of the center of the cylinder. The fluid flow can be characterized with a Reynolds number defined as

$$Re = \frac{u_{avg} d}{v} \tag{3}$$

where v is assumed to be $10^{-2}\ cm^2\ s^{-1}$ [18] and u_{avg} is the average velocity.

The Reynolds numbers of interest in the present study are between 40 and 500. The primitive-variable form of the continuity and momentum equations are solved using a finite element procedure detailed in Wasfy *et al.* [19]:

$$\frac{\partial u_x}{\partial t} + u_x \frac{\partial u_x}{\partial x} + u_y \frac{\partial u_x}{\partial y} = -\frac{1}{\rho}\frac{\partial P}{\partial x} + v\left(\frac{\partial^2 u_x}{\partial x^2} + \frac{\partial^2 u_x}{\partial y^2}\right) \tag{4}$$

$$\frac{\partial u_y}{\partial t} + u_x \frac{\partial u_y}{\partial x} + u_y \frac{\partial u_y}{\partial y} = -\frac{1}{\rho}\frac{\partial P}{\partial y} + v\left(\frac{\partial^2 u_y}{\partial x^2} + \frac{\partial^2 u_y}{\partial y^2}\right) \tag{5}$$

$$\frac{\partial u_x}{\partial x} + \frac{\partial u_y}{\partial y} = 0. \tag{6}$$

The standard Galerkin approximation which reduces to a central difference type of scheme is used. A semi-explicit procedure with equilibrium iterations at each time-step is used. Even though the flow is incompressible we solve the compressible flow equations in their incompressible limit for computational reasons [19]. This approach artificially reduces the propagation speed of a disturbance (which is theoretically infinite for incompressible flows) allowing larger time-steps [20]. The computational domain is divided into quadrilateral elements and conventional bilinear interpolation is used for both the velocity and pressure. The odd–even decoupling of the pressure field is eliminated by the use of a pressure averaging technique. The code has been validated against several steady as well as unsteady benchmark fluid flow problems [19].

The calculations were repeated using about 3700,

6200 and 7800 elements. The difference between the results of the latter two computations was less than 2.5% in time-averaged current density and, hence, all subsequent calculations were carried out with at least 7800 elements. Since measurements are made within nine diameters of the cylinder, the downstream location of the computational domain was truncated at 10 diameters. The appropriateness of this truncation was established by repeating the calculations for other domain lengths and ensuring that the results were the same in the domain of interest.

A fully developed parallel flow with a parabolic velocity profile was specified at the channel inlet:

$$u_x = u_{\max}\left[1-\left(\frac{2y}{h}-1\right)^2\right] \quad \text{and} \quad u_y = 0. \tag{7}$$

The pressure at the channel exit was assumed uniform across the channel height. No-slip conditions for velocity were specified at both the upper and lower walls as well as the cylinder boundary: $u_x = u_y = 0$.

The electrode length $2L$ is much smaller than the computational domain used in the fluid simulations. A separate mesh was, therefore, used for the mass-transfer calculations. The velocity components in the mass-transfer calculations were approximated by their first terms in Taylor series expansion in distance y from the wall:

$$u_x = \beta(x,t)y \quad \text{and} \quad u_y = -\frac{1}{2}\frac{\partial\beta}{\partial x}y^2 \tag{8}$$

where

$$\beta(x,t) = \left.\frac{\partial u_x}{\partial y}\right|_{y=0}$$

was determined from the flow simulations. These velocity components satisfy the continuity equation as well as the no slip boundary conditions.

With these approximations, the concentration field near the electrode is given by

$$\frac{\partial c}{\partial t}+\beta y\frac{\partial c}{\partial x}-\frac{1}{2}\frac{\partial\beta}{\partial x}y^2\frac{\partial c}{\partial y}=D\left(\frac{\partial^2 c}{\partial x^2}+\frac{\partial^2 c}{\partial y^2}\right). \tag{9}$$

At the flow exit, the normal concentration gradient is set to zero. At the flow inlet and large distances from the electrode, the concentration is set at the bulk value. The concentration is set to zero on the electrode surface.

The rate of mass transfer to the electrode is reported in terms of a Nusselt number:

$$Nu = -\frac{1}{2\tau L c_\infty}\int_0^\tau\int_{-L}^{L}\left.\frac{\partial c}{\partial y}\right|_{\text{electrode}}\mathrm{d}x\,\mathrm{d}t \tag{10}$$

where τ is the sample time. When the fluid velocity is periodic, τ can be taken as the period of oscillation. The Nusselt number can be related through Fick's and Faraday's laws to the measured time-averaged current density i_{avg}

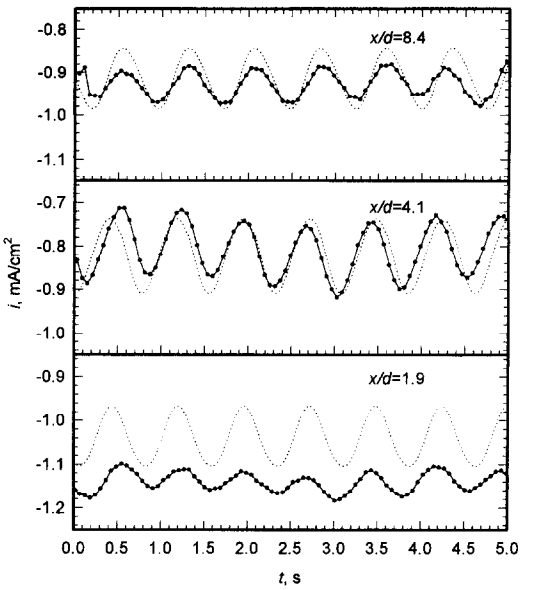

Fig. 3. Experimental and simulated time variation of current density for a sensor placed at three locations (with $d/h = 0.25$ and $b/h = 0.5$). The solid lines are experimental results at $Re = 110$. The dashed lines are the simulated results at $Re = 100$.

$$Nu = \frac{-i_{\text{avg}}L}{FDc_\infty}. \tag{11}$$

RESULTS

It is known that a bluff body in a fluid flow generates a periodic wake in a certain range of Re [13]. Thus, the mass-transfer rate measured by the sensor is also a function of time. Temporal variations of the current density for $Re = 110$ are shown in Fig. 3. Only the quasisteady results, after the initial time transient has disappeared, are shown. The blocking cylinder with $d/h = 0.25$ was placed at the channel center ($b/h = 0.5$). The current density is shown for a sensor located at $x/d = 8.4$, 4.1 and 1.9. The simulated current densities for $Re = 100$ are also shown. The relative variation in the time-average current density was less than 2%. For clarity, error bars are omitted from this and all subsequent figures. Measurement errors are discussed at the end of this section.

Both experiments and simulation indicate that the frequency is the same for all three positions. The oscillation amplitude increases with distance downstream of the cylinder and reaches a maximum near $x/d = 4.1$. Beyond this region, the amplitude decreases. For most simulations, there is reasonable agreement with experiment in frequency and average current density. Simulations, however, tend to overpredict the amplitude of the temporal oscillations in the current density.

The time variation of the current density for $Re = 180$ with a larger blocking cylinder ($d/h = 0.51$)

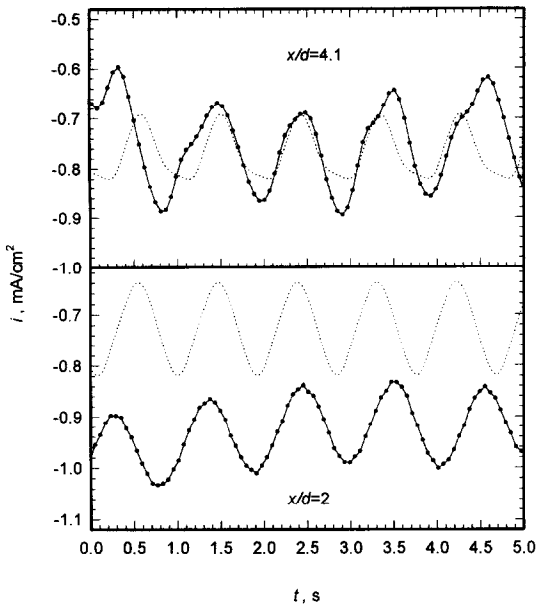

Fig. 4. Experimental and simulated time variation of current density for a sensor placed at $x/d = 2.0$ and 4.1. The solid lines are the experimental results ($d/h = 0.51$, $b/h = 0.5$ and $Re = 180$). The dashed lines are the simulated results ($d/h = 0.5$, $b/h = 0.5$ and $Re = 188$).

placed at the channel center is shown in Fig. 4 for sensor locations of $x/d = 4.1$ and 2.0. Simulated results are again shown for comparison. Time variations of the current density for the sensor located at $x/d = 0.9$ were small and are not reported. Discrepancies between experiments and simulation occur at positions close to the cylinder, where current density varies sharply with position.

Current densities were recorded as a function of time for a large number of flow rates. For $Re < 50$, the mass-transfer rate was steady. When $Re > 200$, more than one frequency was encountered. In the range $50 < Re < 200$, only one dominant frequency was observed. The frequency of oscillation f is a function of Re. The experimental and simulated frequency as a function of Re for both $d/h = 0.25$ and $d/h = 0.51$ ($d/h = 0.5$ in the simulation) are shown in Fig. 5. The frequencies were measured at all three locations downstream of the cylinder positioned at $b/h = 0.5$. Both experiments and simulation show that the frequency of vortex shedding for $d/h = 0.51$ is smaller than that for $d/h = 0.25$.

The shedding frequency is often expressed as a Strouhal number, defined as

$$S = \frac{fd}{u_{avg}}. \tag{12}$$

For all flow rates where the periodicity was at a single dominant frequency the measured Strouhal numbers are 0.27 ± 0.02 and 0.49 ± 0.01 for $d/h = 0.25$ and 0.51, respectively. The corresponding values for simulations are 0.29 and 0.51.

The experimental results can be summarized by

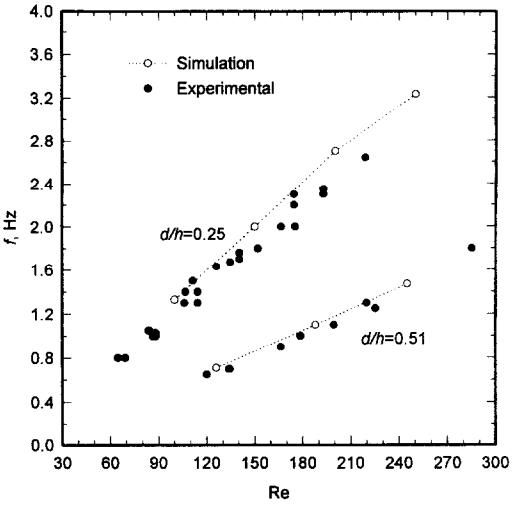

Fig. 5. Variation of oscillation frequency as function of Reynolds number for two cylinder diameters. The simulation (dashed line) with the larger cylinder is performed for $d/h = 0.5$ while experiments (filled circles) were performed with $d/h = 0.51$.

plotting the Nusselt number Nu normalized with Nu_{no} as a function of the flow rate. The Nusselt number Nu_{no} is given by the Leveque solution [20] when there is no cylinder present in the channel

$$Nu_{no} = 1.165\left(\frac{L}{h}\right)^{2/3} Sc^{1/3} Re_h^{1/3}. \tag{13}$$

The normalization factors out approximately the dependence on flow rate. In this manner, the discrepancies between experiment and theory can be illustrated. When $Nu/Nu_{no} > 1$, the cylinder enhances the mass-transfer rate.

Figure 6 shows the normalized Nusselt number as a function of Re at $x/d = 4.1$. The cylinder (with

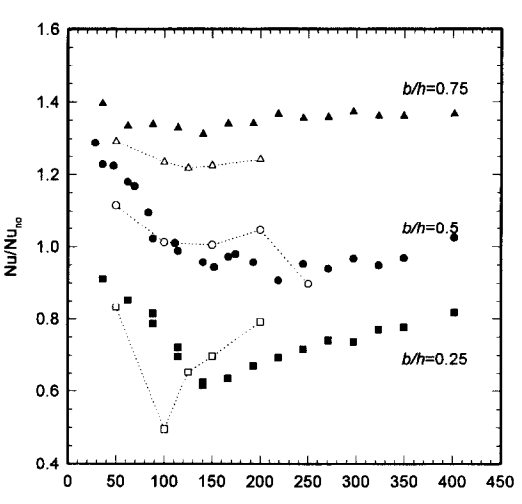

Fig. 6. Effect of Re on the mass transfer rate for a sensor placed at $x/d = 4.1$. Nu_{no} is the Nusselt number in the absence of the cylinder. The dashed lines are simulated results, and the filled symbols are experimental results.

$d/h = 0.25$) was placed at $b/h = 0.25$, 0.5 and 0.75. At $b/h = 0.25$, Nu/Nu_{no} decreases to a minimum at $Re \approx 150$ and then increases to a plateau, but at all Re, Nu is less than that which would be obtained with no cylinder. At $b/h = 0.5$, the mass-transfer enhancement decreases with increasing Re, until $Re \approx 150$. For larger Re, the mass-transfer rate is roughly the same as if there is no cylinder. When the cylinder is away from the wall with $b/h = 0.75$, $Nu/Nu_{no} = 1.35$ and is independent of Re. For the case of $b/h = 0.25$, the simulations predict that a minimum in Nu/Nu_{no} occurs at $Re \approx 100$, instead of the measured value of 135.

When the sensor is placed at $x/d = 1.9$, the normalized Nusselt number behaves as shown in Fig. 7. It shows a sharp maximum at $Re \approx 120$ when the cylinder is placed at $b/h = 0.25$. For this cylinder position, $Nu < Nu_{no}$ at most Re except near the maximum. An approximately 30–35% enhancement in mass-transfer rate is measured with the cylinder placed at $b/h = 0.5$ or 0.75. When $Re < 150$, the enhancement is larger with $b/h = 0.5$ than with $b/h = 0.75$. The reverse is true when $Re > 150$. The agreement between the simulations and experiment is particularly poor at $b/h = 0.25$ for a Reynolds number of 150. For these conditions, simulations show the presence of a recirculation region, the onset of which roughly coincides with the measurement location. This is associated with a vanishing mean shear and a high amplitude of fluctuation in the shear. The disagreement between the experiment and computation is perhaps due to the simulation's inability to capture accurately the variation with Reynolds number of the position of the recirculation region.

Figure 8 shows the variation of the normalized Nusselt number when the sensor is placed at the furthest downstream position $x/d = 8.4$. At $b/h = 0.25$ for $Re < 300$, the cylinder decreases the rate from that obtained with no cylinder. When $Re < 150$, the mass-transfer enhancement is about the same for both cylinder positions of $b/h = 0.5$ and 0.75. As Re increases, the greatest enhancement is obtained when the cylinder is placed at the center.

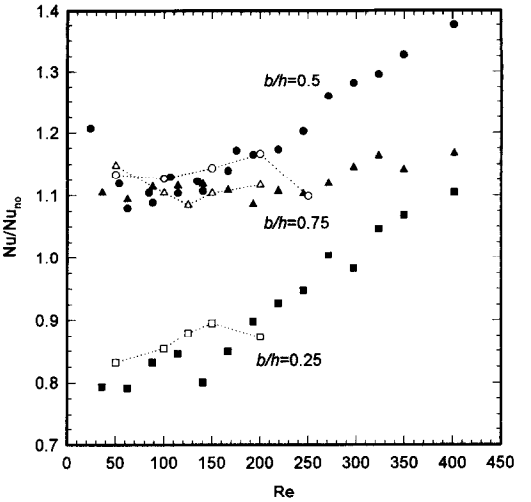

Fig. 8. Effect of Re on the mass transfer rate with the sensor placed at $x/d = 8.4$. The dashed lines are simulated results. The filled symbols are the experimental results.

It may be interesting to compare the mass-transfer rate at different sensor locations for a given cylinder position. When the cylinder is positioned at the center, the lowest mass-transfer rate is obtained at $x/d = 4.1$ while the highest rate was measured at $x/d = 1.9$. The mass-transfer rate is related to the shear at the wall. Figure 9 shows the simulated spatial variation of time-averaged wall shear β_{avg} for $Re = 100$. The corresponding i_{avg} is also shown. Experimental results at four locations with $Re = 110$ are shown for comparison. The shear is at a maximum slightly downstream of the cylinder center. It decreases sharply to a mini-

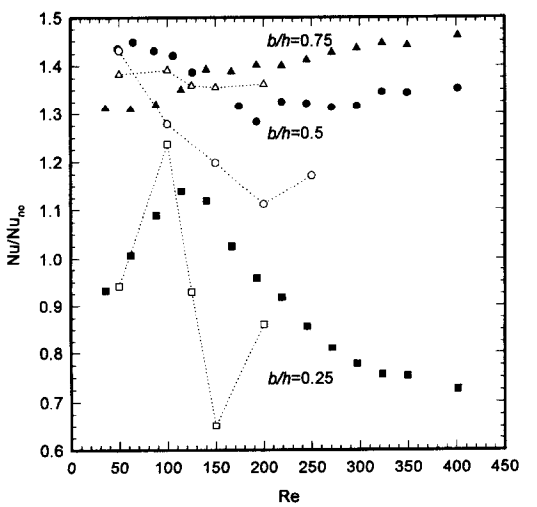

Fig. 7. Effect of Re on the mass transfer rate with the sensor placed at $x/d = 1.9$. The dashed lines are simulated results. The filled symbols are the experimental results.

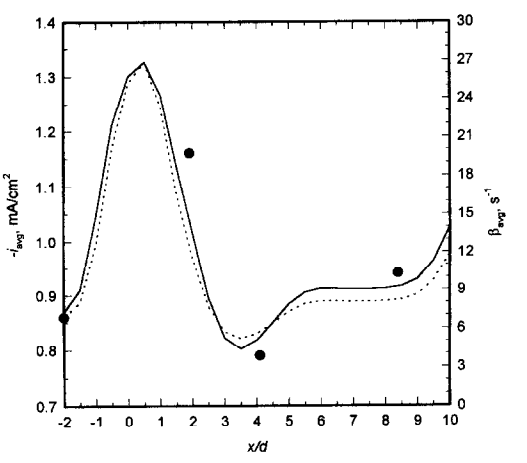

Fig. 9. Spatial variation of simulated wall shear (dashed line) and time-averaged current density downstream of a cylinder ($b/h = 0.5$ and $d/h = 0.25$) at $Re = 100$. The experimental results (symbols) are reported for $Re = 110$. The point at $x/d = -2$ is obtained in the absence of the cylinder.

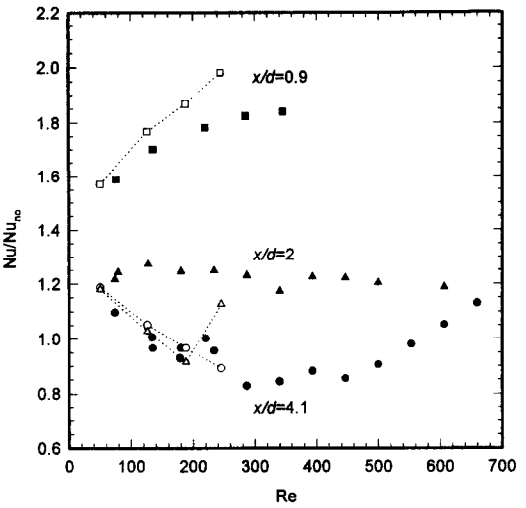

Fig. 10. Effect of Re on the mass transfer rate with a cylinder (with $d/h = 0.51$) located at the channel center. The simulation is performed with $d/h = 0.5$. The open-symbols are the simulated results. The filled symbols are the experimental results.

mum at around $x/d = 4.1$, and then it increases to a nearly constant shear. The current density follows the same shape. The sharp variation of the shear with position in the cylinder region is believed to be the reason that the largest discrepancy between experiment and simulations occurs near the cylinder.

Figure 10 shows the normalized Nusselt number at three locations downstream of a cylinder with $d/h = 0.51$. At $x/d = 0.9$, the mass-transfer rate is enhanced by around 60–80%. At $x/d = 2$, a nearly constant enhancement of 20% was measured. A minimum normalized mass-transfer rate is again measured at $x/d = 4.1$. At this location, Nu/Nu_{no} is at a minimum near $Re = 300$.

Error analysis

Experiments were performed at a room temperature of 23 ± 2°C over a period of three month. Repetition of the experiments from day to day shows the measured average current density i_{avg} is reproducible to within $\pm 0.02 i_{avg}$. The average volumetric flow rate is estimated to be measured within $\pm 0.002Q$. Likewise, the frequency of the current signal is known to within $\pm 0.03f$.

Since the kinematic viscosity varies with temperature [27], the uncertainty in the reported Reynolds number is $\pm 0.05Re$. Likewise, the diffusivity variations with temperature, introduce an uncertainty in the Nusselt number of $\pm 0.05Nu$. The uncertainty in the position of the cylinder x/d is ± 0.11 and ± 0.06 for $d/h = 0.25$ and 0.51, respectively. Other uncertainties are considered to be relatively minor.

DISCUSSION

The Strouhal numbers found in this channel are higher than those obtained for a cylinder in a free stream, where the Strouhal number is about 0.2 [13]. To our knowledge there are no other measurements available in a confined channel. Previous computer simulations [21] with a cylinder in a confined channel ($d/h = 0.24$) placed slightly off center ($b/h = 0.49$), predict that the Strouhal number is 0.3 for $Re = 100$, in reasonable agreement with the present experimental and simulation results.

A snapshot of the streamlines (for $Re = 100$, $d/h = 0.25$ and $b/h = 0.5$) is shown in Fig. 11. The upstream influence of the cylinder is confined to a small region ahead of the cylinder. Just downstream, a pair of asymmetric vortices oscillate periodically, creating a wake that persists further downstream. There is a region of recirculation near $x/d = 4.1$. The local recirculation is the reason why mass-transfer rate is the lowest at this position. This case illustrates some of the features of the flow and mass-transfer rates. The time-averaged shear is considerably higher below the cylinder over a region extending about 2.5 diameters downstream of the cylinder primarily due to the blockage induced acceleration of the flow. As the flow decelerates, the adverse pressure gradient causes flow separation, forming a recirculation region that leads to a low time-averaged shear.

The location of the recirculation region varies with

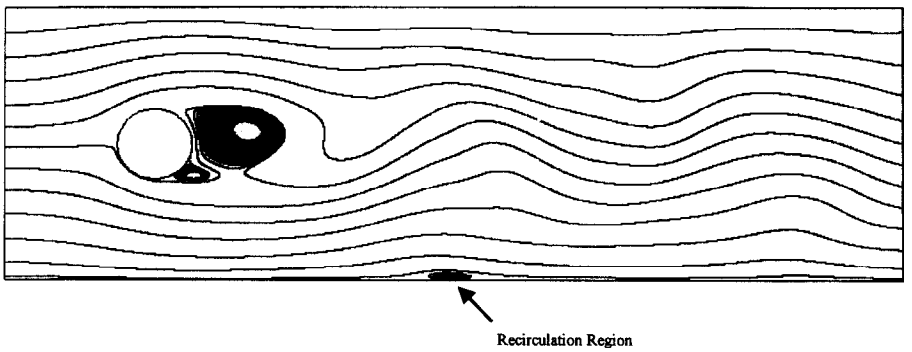

Fig. 11. Snapshot of the streamlines with a cylinder ($d/h = 0.25$) placed at $b/h = 0.5$ for $Re = 100$. The position of the recirculation region, indicated by the arrow, depends on Re. When the recirculation region is above the sensor, the mass-transfer rate decreases.

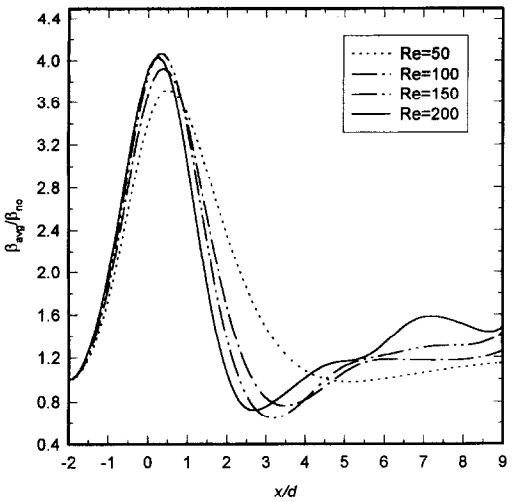

Fig. 12. Normalized shear along the wall at different *Re*. The local recirculation region (the region showing minimum shear) is shifted toward the cylinder with increasing *Re*. Here $d/h = 0.25$ and $b/h = 0.5$.

Reynolds numbers and moves upstream with increasing *Re* in the range of 50–200. This is shown in Fig. 12, where the normalized wall shear β_{avg}/β_{no} is shown as a function of position for various *Re*, where β_{no} is the wall shear in the absence of a cylinder. If the location where β_{avg}/β_{no} is less than unity is taken to be a measure of incipient recirculation, then this region moves further upstream with increasing Reynolds numbers. For a sensor located at $x/d = 4.1$ we observe that β_{avg}/β_{no} first reduces as the recirculation region passes over the sensor and then increases back again. This would correspond to an initial reduction in mass-transfer enhancement followed by a recovery as observed in Fig. 6.

The numerical simulations are all carried out by making an assumption of two-dimensionality. The transition to three-dimensionality in the near wake of a cylinder has been observed to occur at a Reynolds number of about 200 in the absence of confining walls [13, 24]. We report here numerical simulations for Reynolds numbers as high as 250. The 2-D simulations of flows in the *Re* range of between 200 and 250 can perhaps be utilized for qualitative comparison. This is justified based on the work of Henderson [25] and Braza and Persillon [26], who report that 2-D simulations never deviate by more than 20% from the 3-D simulations in this range of Reynolds numbers.

CONCLUSIONS

The rate of mass transfer in a flow channel in the presence of a blocking cylinder depends on the separation distance between the plate and the cylinder, the position downstream of the cylinder, the blockage ratio as well as the flow rate. When $b/h > 0.5$, the mass-transfer rate is enhanced significantly. Maximum enhancement occurs close to the cylinder while the minimum mass-transfer rate is observed in regions of recirculation. Periodic oscillations were observed experimentally for $50 < Re < 200$. The Strouhal number is found to be larger than that measured in a free stream. Two-dimensional simulations of the fluid flow and mass-transfer are in reasonable agreement with experiment.

Acknowledgements—This work was supported by the National Science Foundation under Grant no. CTS-93-15991. Partial support was also provided by the Exxon Education Foundation. The authors would like to thank Dr Tamer Wasfy for the development and continued assistance in the use of the fluid flow solver.

REFERENCES

1. Romankiw, L. T., Acosta, R. E. and Powers, J. V., A paddle-type cell for plating of electronic circuits. *Journal of the Electrochemical Society*, 1977, **124,** 301C.
2. Schwartz, D. T., Higgins, B. G. and Stroeve, P., Mass-transfer studies in a plating cell with a reciprocating paddle. *Journal of the Electrochemical Society*, 1987, **134,** 1639–1645.
3. Thomas, D. G., Forced convection mass transfer: part II. Effect of wires located near the edge of the laminar boundary layer on the rate of forced convection from a flat plate. *A.I.Ch.E. Journal*, 1965, **11,** 848–852.
4. Thomas, D. G., Forced convection mass transfer: part III. Increased mass transfer from a flat plate caused by the wake from cylinders located near the edge of the boundary layer. *A.I.Ch.E. Journal*, 1966, **12,** 124–130.
5. Isaacson, M. S. and Sonin, A. A., Sherwood number and friction factor correlations for electrodialysis systems, with application to process optimization. *Industrial Engineering Chemistry, Process Design Developments*, 1976, **15,** 313–321.
6. Sonin, A. A. and Isaacson, M. S., Optimization of flow design in forced flow electrochemical systems, with special application to electrodialysis, *Industrial Engineering Chemistry, Process Design Development*, 1974, **13,** 241–248.
7. Zheng, G. S. and Worek, W. M., Methods of heat and mass transfer enhancement in film evaporation. *International Journal of Heat and Mass Transfer*, 1996, **39,** 97–108.
8. Berger, F. P. and Hau, K.-F. F.-L., Local mass/heat transfer distribution on surfaces roughened with small square ribs. *International Journal of Heat and Mass Transfer*, 1979, **22,** 1645–1656.
9. Karniadakis, E., Mikic, B. B. and Patera, A. T., Minimum-dissipation transport enhancement by flow destabilization: Reynolds' analogy revisited. *Journal of Fluid Mechanics*, 1988, **192,** 365–391.
10. Kozlu, H., Mikic, B. B. and Patera, A. T., Minimum-dissipation heat removal by scale-matched flow destabilization. *International Journal of Heat and Mass Transfer*, 1988, **31**(10), 2023–2032.
11. Yesilyurt, S. and Patera, A., ICASE Report no. 93-50, NASA, Langley Research Center, August 1993.
12. Myrum, T. A., Acharya, S., Sinha, S. and Qui, X., The effect of placing vortex generators above ribs in ribbed ducts on the flow, flow temperature, and heat transfer behavior. *Journal of Heat Transfer*, 1996, **118,** 294–300.
13. Williamson, C. H. K., Vortex dynamics in the cylinder wake. *Annual Review of Fluid Mechanics*, 1996, **28,** 477–539.
14. Mitchell, J. E. and Hanratty, T. J., A study of turbulence at a wall using an electrochemical wall shear-stress meter. *Journal of Fluid Mechanics*, 1966, **26,** 199–221.

15. Hanratty, T. J. and Campbell, J. A., Measurements of wall shear stress. In *Fluid Mechanics Measurements*, 2nd edn, ed. Richard J. Goldstein. Taylor and Francis, 1996, Chapter 11.
16. Perry, R. H. and Green, D., *Perry's Chemical Engineers' Handbook*, 6th edn. McGraw-Hill, New York, 1984, pp. 5–35.
17. Natarajan, N. M., and Lakshmanan, Laminar flow in rectangular ducts: prediction of velocity profiles and friction factor. *Indian Journal of Technology*, 1972, **10**, 435–438.
18. Newman, J., *Electrochemical Systems*, 2nd edn. Prentice-Hall, Englewood Cliffs, NJ, 1991.
19. Wasfy, M., West, A. C. and Modi, V., Parallel finite element computation of unsteady incompressible flows. *International Journal for Numerical Methods in Fluids* 1996 (submitted).
20. Chorin, J., A numerical method for solving incompressible viscous flow problems. *Journal of Computational Physics*, 1967, **2**, 12–26.
21. Ferziger, J. H. and Peric, M., *Computational Method for Fluid Dynamics*. Springer, Berlin, 1996.
22. Williamson, H. K., The existence of two stages in the transition to three-dimensionality of a cylinder wake. *Physics of Fluids*, 1988, **31**(11), 3165–3168.
23. Zienkiewicz, C. and Taylor, R. L., *The Finite Element Method*, 4th edn, Vol. 2. McGraw-Hill, London, 1991, pp. 444–445.
24. Karniadakis, E. and Triantafyllou, G. S., Three-dimensional dynamics and transition to turbulence in the wake of bluff objects. *Journal of Fluid Mechanics*, 1992, **238**, 1–30.
25. Henderson, D., Unstructured spectral element methods: parallel algorithms and simulations, Ph.D. thesis. Princeton University, 1994.
26. Braza, M. and Persillon, H., Prediction of certain transition characteristics in the wake of a cylinder. *Proceedings of the IUTAM Conference of Bluff Body Wake Instabilities*, eds Eckelman *et al.* Springer, Berlin, 1992.
27. Incropera, F. P. and Dewitt, D. P., *Fundamentals of Heat Transfer*. Wiley, New York, 1981.